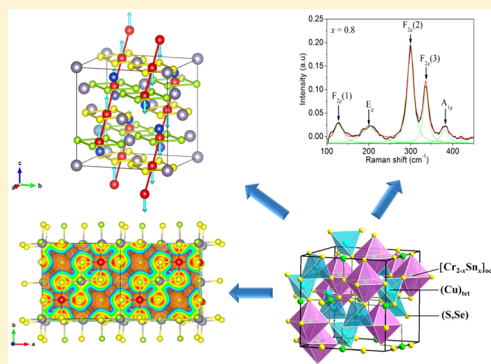


(Cu)_{tet}(Cr_{2–x}Sn_x)_{oct}S_{4–y}Se_y Spinels: Crystal Structure, Density Functional Theory Calculations, and Magnetic Behavior

Silvana Moris,[†] Paulina Valencia-Gálvez,[‡] José Mejía-López,[§] Octavio Peña,[⊥] Patricia Barahona,^{*,||} and Antonio Galdámez^{*,‡,§}[†]Vicerrectoría de Investigación y Postgrado, Universidad Católica del Maule, Talca, Chile 3460000[‡]Departamento de Química, Facultad de Ciencias, Universidad de Chile, Santiago, Chile 7800003[§]Centro de Investigación en Nanotecnología y Materiales Avanzados CIEN-UC, Facultad de Física, Pontificia Universidad Católica de Chile, CEDENNA, Santiago, Chile 8320000[⊥]Univ. Rennes, CNRS, ISCR (Institut des Sciences Chimiques de Rennes), UMR 6226, F-35000 Rennes, France^{||}Facultad de Ciencias Básicas, Universidad Católica del Maule, Talca, Chile 3460000

Supporting Information

ABSTRACT: A new series of (Cu)_{tet}[Cr_{2–x}Sn_x]_{oct}S_{4–y}Se_y compounds was prepared by solid-state reaction at high temperature. Determination of the crystal structures by single-crystal X-ray diffraction revealed that CuCr_{1.0}Sn_{1.0}S_{2.1}Se_{1.9}, CuCr_{1.2}Sn_{0.8}S_{2.1}Se_{1.9}, CuCr_{1.3}Sn_{0.7}S_{2.2}Se_{1.8}, and CuCr_{1.5}Sn_{0.5}S_{2.2}Se_{1.8} crystallize in a normal spinel-type structure (cubic *Fd* $\bar{3}m$ space group). The powder X-ray diffraction patterns and Rietveld refinements of nominal CuCr_{2–x}Sn_xS₂Se₂ ($x = 0.2, 0.4, 0.6, 0.8$, and 1.0) were consistent with single-crystal X-ray diffraction data. Raman scattering analysis revealed that the A_{1g} , E_g , and three F_{2g} vibrational modes were observed in the spectra. The signal at ~ 382 cm^{–1}, corresponding to the A_{1g} mode, is attributed to symmetrical stretching of the chalcogen bond with respect to the tetrahedral metal. The samples with $x = 0.2$ and 0.4 exhibited ferromagnetic behavior, characterized by large positive θ values of +261 and +189 K, respectively. In contrast, antiferromagnetic (AF) behavior was observed for CuCrSnS₂Se₂ with a Néel temperature (T_N) of 18.8 K and a θ value of –36.0 K. Density functional theory (DFT) and effective magnetic moments ($\mu_{\text{eff}}/\mu_{\text{theo}}$) experimentally measured showed that the Sn ion is in oxidation state of 4+, i.e., diamagnetic behavior. DFT calculations revealed that the most stable magnetic state of CuCr_{1.0}Sn_{1.0}S₂Se₂ was AF with exchange constants for first- and second-neighbor interactions of $J_1 = 56.22$ cm^{–1} and $J_2 = -33.88$ cm^{–1}. Thus, the AF interactions between ferromagnetic chains in CuCr_{1.0}Sn_{1.0}S₂Se₂ originate from the presence of diamagnetic Sn cations.



INTRODUCTION

Spinels are compounds with AB₂X₄ stoichiometry (cubic *Fd* $\bar{3}m$ space group), where A and B are cations and X is the anion.^{1,2} The normal spinel given by the chemical formula (A)_{tet}[B₂]_{oct}X₄ (X = O, S, or Se) consists of A occupying tetrahedral sites and B in octahedral ones. In spinels, the X anions, bonded to A and B cations, form a cubic closest-packing arrangement.

Thiospinels and selenospinels (X = S and X = Se, respectively) with normal spinel-type structures have generated great interest because of their pressure-induced phase transitions and magnetic and transport properties.^{3–5} Spinels based on Cr have been shown to possess magnetoresistance, which refers to a change in the electrical resistance of certain materials in the presence of a magnetic field.⁶ This property has been the focus of various studies for its potential use in data storage and electronic devices.^{7,8} In contrast, thiospinels and selenospinels undergo pressure-induced phase transitions toward a spinel-distorted, monoclinic structure or a LiTiO₂-

type structure.^{9,10} In addition, CuCr₂S₄ and CuCr₂Se₄ are metallic and ferromagnetic with Curie temperatures (T_C) of 380 and 420 K, respectively.¹¹ The magnetic properties in CuCr₂S₄ and CuCr₂Se₄ can be attributed to the double exchange model between Cr³⁺ and Cr⁴⁺.^{12,13} Large negative magnetoresistance has also been reported in ferromagnetic CuCrZrS₄.¹⁴

The magnetic properties of CuCr₂S₄ and CuCr₂Se₄ can be modified by replacing the metal ions in the tetrahedral positions (A) or the Cr subarray with diamagnetic ions. The experimental magnetic phase diagram of (Cu)_{tet}[Cr_{2–x}Ti_x]_{oct}S₄ have been published by Kariya et al.¹⁵ Their experimental results suggest that the evolution from ferromagnetic behavior to a spin-glass regime is due to magnetic frustrations triggered by the chemical substitutions of chromium by titanium. In addition, the physical properties of CuCr₂S₄ have been

Received: June 24, 2019

explained by assuming that the oxidation states in this compound can be represented as $\text{Cu}^+\text{Cr}^{3+}\text{Cr}^{4+}\text{S}_2^{2-}$; thus, electrical properties and ferromagnetic behavior can be attributed to double exchange between Cr^{3+} and Cr^{4+} .^{12,13} Furthermore, the magnetic properties of CuCr_2Se_4 have also been modified by substitution of Cr. The progressive chemical substitution of Cr by Ti in $(\text{Cu})_{\text{tet}}[\text{Cr}_{2-x}\text{Ti}_x]_{\text{oct}}\text{Se}_4$ resulted in various magnetic domains, including a diluted regime and the coexistence of ferromagnetism and a spin-glass regime.¹⁶ $(\text{Cu})_{\text{tet}}[\text{Cr}_{2-x}\text{Sn}_x]_{\text{oct}}\text{Se}_4$ showed evident ferromagnetic behavior at $x = 0.3$, whereas at $x = 0.7$, antiferromagnetic (AF) behavior was observed with a dominant ferromagnetic character in the exchange interactions.¹⁷ Chemical substitutions of Cr, such as in $(\text{Cu})_{\text{tet}}[\text{Cr}_{2-x}\text{M}_x]_{\text{oct}}\text{Se}_4$ spinels, revealed that M exists in the 4+ oxidation state, whereas Cu exists as a diamagnetic Cu^+ cation.^{16–20}

The magnetic and electric properties of thiospinels can also be modified by the degree of Se substitution. For example, the T_C of the ferromagnetic $\text{CuCr}_2\text{S}_{4-y}\text{Se}_y$ spinel systematically increases as the Se (y) content increases.^{21,22} Similarly, changes are induced by chemical substitution of S by Se in the metal insulator CuIr_2S_4 to form $\text{CuIr}_2(\text{S}_{1-y}\text{Se}_y)_4$. The metal–insulator transition occurs at a lower temperature and a full metallic state for $y \geq 0.8$. Notably, the temperature-induced metal–insulator transition for $y \leq 0.15$ is accompanied by a structural transition from a tetragonal to a cubic structure.²³ In this solid solution, the end-member CuIr_2Se_4 exhibits metallic behavior down to 0.5 K. Nagata et al.²³ have suggested that the magnetic properties are changed by adjusting the chalcogenide stoichiometry (S and Se subnetwork) without a significant alteration of the normal cubic-spinel structure. In other cases, however, there is a gradual change in the physical properties. For instance, a decrease in T_C is observed with increasing Se content in ferrimagnetic $\text{MCr}_2\text{S}_{4-y}\text{Se}_y$ ($\text{M} = \text{Fe}, \text{Co}, \text{or Mn}$).²⁴ Likewise, there is a decrease of T_C in the ferrimagnetic spinel series $\text{Cu}_{0.45}\text{Co}_{0.55}\text{Cr}_2\text{S}_{4-y}\text{Se}_y$, but the dependence on the Se content (y) is not linear.

Herein, the structural and magnetic properties of $(\text{Cu})_{\text{tet}}[\text{Cr}_{2-x}\text{Sn}_x]_{\text{oct}}\text{S}_{4-y}\text{Se}_y$ were explored using experimental measurements and density functional theory (DFT) calculations. The crystal structure was confirmed by single-crystal X-ray diffraction (XRD). In these phases, the cell parameter a increased gradually as Cr^{4+} ions were replaced by Sn^{4+} cations, in accordance with Vegard's law. The Cu–X ($X = \text{Se/S}$) distances are intermediate between the Cu–Se and the Cu–S bond lengths of the end-members, and this is attributed to the similar chemical proportions of Se and S. The edge-length distortion (ELD) indices of the $[\text{Cr}_{2-x}\text{Sn}_x]\text{X}_6$ octahedron (1.9–2.3%) were lower than the octahedral distortions of previously reported compounds. The vibrational analysis showed that the A_{1g} , E_g , and three F_{2g} modes were Raman-active. The signals compared very well with the Raman spectra of the thio- and selenospinel end-members. Rietveld analyses, powder X-ray diffraction (PXRD) patterns, backscattered images, and energy-dispersive X-ray spectroscopy (EDS) revealed that the samples were homogeneous within the detection limits. Indeed, all phases were indexed in the $Fd\bar{3}m$ space group (spinel-type). The samples showed an evolution from ferromagnetic to AF behavior. The magnetic measurements and DFT calculations suggested that the oxidation state model is $(\text{Cu}^{1+})_{\text{tet}}[\text{Cr}^{3+}\text{Cr}^{4+}_{1-x}\text{Sn}_x]_{\text{oct}}\text{S}_2\text{Se}_2$. The origin of the AF interaction between ferromagnetic chains in $\text{CuCr}_{1.0}\text{Sn}_{1.0}\text{S}_2\text{Se}_2$

was the chemical substitution of Cr by diamagnetic Sn cations in the normal spinel-type end-member.

2. EXPERIMENTAL SECTION

2.1. Synthesis. Powder samples of $\text{CuCr}_{2-x}\text{Sn}_x\text{S}_2\text{Se}_2$ were prepared by directly combining high-purity elemental powders (99.99%, Aldrich) in stoichiometric amounts (~ 2.0 g of compound). All manipulations were carried out under an Ar atmosphere. The reaction mixtures were sealed in evacuated quartz ampules and placed in a programmable furnace. The ampules were slowly heated from room temperature to 500 °C at a rate of 150 °C/h. They were then heated to 850 °C at a rate of 60 °C/h and held at this temperature for 8 days. Finally, the ampules were slowly cooled to room temperature at a rate of 60 °C/h. Using similar methodology, single crystals were obtained in a horizontal tubular furnace by directly combining high-purity elemental powders (99.99%, Aldrich) in stoichiometric amounts (~ 300 mg of compound) with ~ 2 wt % excess S and Se. The ampules were slowly cooled to room temperature at a rate of 15 °C/h.

2.2. Characterization. Single-crystal XRD data for $\text{CuCr}_{1.0}\text{Sn}_{1.0}\text{S}_{2.1}\text{Se}_{1.9}$ (1) and $\text{CuCr}_{1.2}\text{Sn}_{0.8}\text{S}_{2.1}\text{Se}_{1.9}$ (2) were collected at 150 K with a D8 VENTURE Bruker AXS diffractometer²⁵ using Mo $K\alpha$ radiation ($\lambda = 0.71073$ Å). Single-crystal XRD data for $\text{CuCr}_{1.3}\text{Sn}_{0.7}\text{S}_{2.2}\text{Se}_{1.8}$ (3) and $\text{CuCr}_{1.5}\text{Sn}_{0.5}\text{S}_{2.2}\text{Se}_{1.8}$ (4) were collected at room temperature with a Bruker Smart CCD diffractometer using graphite-monochromated Mo $K\alpha$ radiation ($\lambda = 0.71073$ Å). Data collections were conducted with the Bruker SMART software package.²⁵ Structural refinement was performed with the SHELXL²⁶ and Olex2²⁷ programs. EDS analysis of the single crystals used in XRD experiments (elemental mapping) showed the presence of Cu, Cr, Sn, S, and Se. CSD contains the supplementary crystallographic data for this paper with deposition numbers of 1935201, 1935203, 1935209, and 1935210 for 1–4. The crystallographic data can be obtained free of charge from The Cambridge Crystallographic Data Centre via http://www.ccdc.cam.ac.uk/data_request/cif.

PXRD patterns were collected at room temperature in the range of $5^\circ < 2\theta < 80^\circ$ using a Bruker D8 Advance powder diffractometer (Bruker, Billerica, MA) with $\text{CuK}\alpha$ radiation ($\lambda = 1.54178$ Å). The XRD patterns were indexed using the CHEKCELL program. The data were analyzed by Rietveld refinements performed in the MAUD program.²⁸ LaB_6 powder standard was used to determinate the instrumental profile.

Chemical composition determination and mapping analyses of the samples were performed by EDS and scanning electron microscopy (SEM) using a Tescan Vega 3 scanning electron microscope equipped with a Quantax 400 EDS microanalyser. Cylindrical pellets (6 mm in diameter and ~ 2 mm thick) were uniaxially pressed at $\sim 5 \times 10^8$ Pa. These samples were then mounted on double-sided carbon tape and adhered to an Al specimen holder for analysis.

Raman scattering measurements were conducted on a Witec Alpha 300 System using 532 nm wavelength excitation. The spectrometer was calibrated with a reference single-crystal Si sample (Raman peak at 520.7 cm^{-1}). The spectral data were collected at room temperature in a backscattering configuration in the spectral range of 100–450 cm^{-1} , with a laser spot of ~ 1 μm and laser power of 2 mW.

Magnetic measurements were performed on pelletized powder samples using an MPMS SXL magnetic property measurement system (Quantum Design, San Diego, CA). The magnetic properties of the materials were determined using zero-field-cooled (ZFC) and field-cooled (FC) cycles under low applied magnetic fields (typically 500 Oe).

The electronic structure calculations were performed in the DFT framework using the Vienna Ab Initio Simulation Package (VASP),^{29,30} which implements a DFT code^{31,32} based on a pseudopotential plane-wave expansion. The projector augmented wave (PAW) method^{33,34} and the Perdew–Burke–Ernzerhof (PBE) exchange–correlation functional³⁵ for the spin-polarized generalized gradient correction were used. The 3d⁵ and 4s¹ electrons of Cr, the 5s² and 5p² electrons of Sn, the 4s² and 4p⁴ electrons of Se, the 3s²

Table 1. Crystallographic Data for $(\text{Cu})_{\text{tet}}[\text{Cr}_{2-x}\text{Sn}_x]_{\text{oct}}\text{S}_{4-y}\text{Se}_y$ Spinel-Type

	$\text{CuCr}_{1.0}\text{Sn}_{1.0}\text{S}_{2.1}\text{Se}_{1.9}$	$\text{CuCr}_{1.2}\text{Sn}_{0.8}\text{S}_{2.1}\text{Se}_{1.9}$	$\text{CuCr}_{1.3}\text{Sn}_{0.7}\text{S}_{2.2}\text{Se}_{1.8}$	$\text{CuCr}_{1.5}\text{Sn}_{0.5}\text{S}_{2.2}\text{Se}_{1.8}$
Crystal Data				
crystal system, space group	cubic, $Fd\bar{3}m$			
a (Å)	10.398(2)	10.3432 (8)	10.292(7)	10.255(7)
V (Å ³)	1124.2(7)	1106.5(3)	1090(2)	1079(2)
μ (mm ^{−1})	22.87	22.30	22.15	21.97
crystal size (mm)	$0.07 \times 0.04 \times 0.04$	$0.06 \times 0.06 \times 0.05$	$0.13 \times 0.13 \times 0.06$	$0.15 \times 0.08 \times 0.06$
Data Collection				
$T_{\text{min}}, T_{\text{max}}$	0.3119, 0.7485	0.6174, 0.7469	0.5512, 1.0000	0.4922, 1.0000
no. of measured	1230	1229	2936	1790
R_{int}	0.0329	0.0252	0.0520	0.0610
no. of independent reflections	115	123	98	96
$(\sin \theta/\lambda)_{\text{max}}$ (Å ^{−1})	0.732	0.755	0.694	0.696
Refinement				
$R_1[F^2 > 2\sigma(F^2)], R_1$	0.0136, 0.0188	0.0121, 0.0144	0.0150, 0.0175	0.0234, 0.0308
$wR_2(F^2), wR_2$	0.0317, 0.0307	0.0280, 0.0260	0.0341, 0.0362	0.0402, 0.0379
no. of reflections	95	104	87	80
no. of parameters	10	10	10	10
GOF	0.986	0.607	1.028	1.224
$\Delta\rho_{\text{max}}, \Delta\rho_{\text{min}}$ (e Å ^{−3})	0.96, −0.51	0.52, −0.65	0.34, −0.69	0.50, −0.60

and $3p^4$ electrons of S, and the $3d^{10}$ and $4s^1$ electrons of Cu were treated as valence electrons. The energy cutoff was set at 280 eV, and the electronic energy convergence criterion was set at 10^{-7} eV to obtain a reliable description of these systems. The Monkhorst–Pack scheme was used to discretize the Brillouin-zone (BZ) integrations³⁶ with a $4 \times 4 \times 4$ mesh, which corresponds to a set of 32 special k points in the irreducible BZ for spinel-type structures. Symmetry unrestricted optimizations of both geometry and spin were performed using conjugate gradient and quasi-Newtonian methods until all force components were less than 0.006 eV/Å.

3. RESULTS AND DISCUSSION

3.1. Crystal Structure Analysis. To characterize the crystal structures of the $\text{CuCr}_{2-x}\text{Sn}_x\text{S}_{4-y}\text{Se}_y$ solid solutions, suitable single crystals were selected and analyzed on a conventional diffractometer. Different structural models for the permutations of the metal and chalcogen atom positions were refined. For each crystal, two models were considered: (1) Cu and Sn cations sharing the tetrahedral (A) sites and (2) Cr and Sn cations sharing the octahedral [B] sites. These models were based on linear functions constraining the Sn, Cu, and Cr atoms to $16d$ and $8a$ sites. For the tetrahedral cation site, the sum of the site occupation factors (SOF) was constrained to equal 1 (fully occupied) for $8a = (1-x)\text{Cu} + x\text{Sn}$. The sum of the SOF in the octahedral cation site was constrained to equal 2 (fully occupied) for $16d = (2-y)\text{Cr} + y\text{Sn}$. Furthermore, for the chalcogenide site (in both models), the sum of the SOF was constrained to equal 1 (fully occupied) for $32e = (4-y)\text{S} + y\text{Se}$. The Sn and Cr atoms were constrained to have equivalent atomic displacement parameters (ADPs), as were the S and Se atoms (Table S1). A careful examination of the structural details, such as the ADPs and the R and wR_2 indices provided a strong indication of crystal structure final refinement. The best convergence refinements were obtained for four single crystals in model 2. The crystal data, experimental details, and conditions are summarized in Table 1. The SEM backscattered electron images (mapping) and EDS analysis showed the elemental compositions of the crystals (Figure S1). For example, the experimental results revealed a Cu/Cr/Sn/S/Se ratio of $\sim 1.0/1.1/0.7/2.2/1.7$ for one single crystal (average of three acquisitions).

$(\text{Cu})_{\text{tet}}[\text{Cr}_{2-x}\text{Sn}_x]_{\text{oct}}\text{S}_{4-y}\text{Se}_y$ compounds crystallize in the normal spinel-type structure ($Fd\bar{3}m$ space group). The cell parameter a in $\text{CuCr}_{1.0}\text{Sn}_{1.0}\text{S}_{2.1}\text{Se}_{1.9}$ (10.398 Å) has an intermediate value between those of CuCrSnS_4 (10.175 Å)³⁷ and CuCrSnSe_4 (10.672 Å),³⁸ which is attributed to the similar chemical proportions of Se and S. The effective octahedral ionic radii of Cr^{3+} , Cr^{4+} , and Sn^{4+} published by Shannon³⁹ are 0.62 Å, 0.55 Å, and 0.69 Å, respectively.³⁹ Accordingly, the cell parameter a increased gradually as the Cr^{4+} ions were replaced by the larger Sn^{4+} cations in $(\text{Cu})_{\text{tet}}[\text{Cr}_{2-x}\text{Sn}_x]_{\text{oct}}\text{S}_{4-y}\text{Se}_y$. These cell parameters obey Vegard's law.

The Cu–X ($X = \text{S}/\text{Se}$) distances in $(\text{Cu})_{\text{tet}}[\text{Cr}_{2-x}\text{Sn}_x]_{\text{oct}}\text{S}_{4-y}\text{Se}_y$ ranged from 2.3210(2) Å to 2.3288(5) Å. These distances are intermediate between the Cu–Se bond lengths in $(\text{Cu})_{\text{tet}}[\text{Cr}_{2x}\text{Sn}_x]_{\text{oct}}\text{Se}_4$ (2.3832–2.3947 Å) and the Cu–S bond lengths in thiospinels $(\text{Cu})_{\text{tet}}[\text{Ti}_{1.7}\text{M}_{0.3}]_{\text{oct}}\text{S}_4$ (2.2583–2.2737 Å). The Cu–X distances were close to the tetrahedral covalent radii published by Pyykkö⁴⁰ for Cu–S (2.313 Å). The $(\text{Cu})\text{X}_4$ tetrahedral was ideal with angles of 109.47° . The $[\text{M}]_{\text{Oh}}\text{X}_6$ octahedral exhibit multication chemical substitutions that caused distortion of the chalcogen subnetwork. The $[\text{Cr/Sn}]_{\text{Oh}}\text{X}$ bond distances ranged from 2.5071(18) Å to 2.5532(7) Å and were comparable to the $[\text{Cr/Sn}]$ –Se bond lengths in $(\text{Cu})_{\text{tet}}[\text{Cr}_{2x}\text{Sn}_x]_{\text{oct}}\text{Se}_4$. All other relevant structural parameters (bond distances and angles) were as expected and in acceptable agreement with those of other thio- and selenospinel compounds.

The crystal structure of $(\text{Cu})_{\text{tet}}[\text{Cr}_{2-x}\text{Sn}_x]_{\text{oct}}\text{S}_{4-y}\text{Se}_y$ solid solutions can be described by two main polyhedra: a $(\text{Cu})_{\text{tet}}\text{X}_4$ tetrahedron and a $[\text{Cr}_{2-x}\text{Sn}_x]_{\text{oct}}\text{X}_6$ octahedron (Figure 1a). Baur⁴¹ evaluated the degree of distortion in the tetrahedra and octahedra using distortion indices.⁴¹ The degree of distortion can be measured by the ELD indices: $\text{ELD} = \frac{100}{12} \sum_{i=1}^{12} \frac{(X-X)_i - \langle X-X \rangle}{\langle X-X \rangle} \%$, where $(X-X)_i$ is chalcogen–chalcogen bond distance and $\langle X-X \rangle$ is the average chalcogen–chalcogen bond distance on the octahedral edge. The $[\text{Cr}_{2-x}\text{Sn}_x]_{\text{oct}}\text{X}_6$ octahedron ELD indices had values ranging from 1.9% to 2.3%, which are lower than the

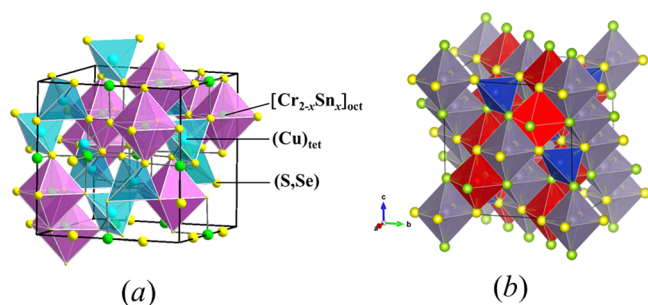


Figure 1. (a) Polyhedral representation of the crystalline structure obtained by single-crystal X-ray diffraction. (b) $\text{CuCrSnS}_2\text{Se}_2$ representation obtained by means of DFT calculations. Red, gray, and blue polyhedra enclose Cr, Sn, and Cu atoms, respectively, whereas green and yellow spheres represent Se and S atoms, respectively.

octahedral distortions in compounds previously reported by our research group, namely, $(\text{Cu})_{\text{tet}}[\text{Cr}_{2-x}\text{Ti}_x]_{\text{oct}}\text{Se}_4$ ¹⁶ and $(\text{Cu})_{\text{tet}}[\text{Cr}_{2-x}\text{Sn}_x]_{\text{oct}}\text{Se}_4$.¹⁷ This decrease in the distortion indices can be explained by the effect of the disorder in the tetrahedral chalcogen 32e (*u,u,u*) sites in a cubic closed-packed array.

3.2. PXRD Patterns, SEM-EDS Analyses, and Raman Scattering. The PXRD patterns of the polycrystalline $(\text{Cu})_{\text{tet}}[\text{Cr}_{2-x}\text{Sn}_x]_{\text{oct}}\text{S}_2\text{Se}_2$ ($x = 0.2, 0.4, 0.6, 0.8$, and 1.0) materials were fully indexed to the $Fd\bar{3}m$ space group (spinel-type structure) and compared with the simulated XRD patterns derived from the single-crystal XRD data (Figure 2). Rietveld refinements were performed using the PXRD data collected at room temperature (Figure S2). The resulting structural model was in good agreement with those obtained using the single-crystal XRD data. No secondary phases or impurity peaks were detected. The *R*-indices were refined to

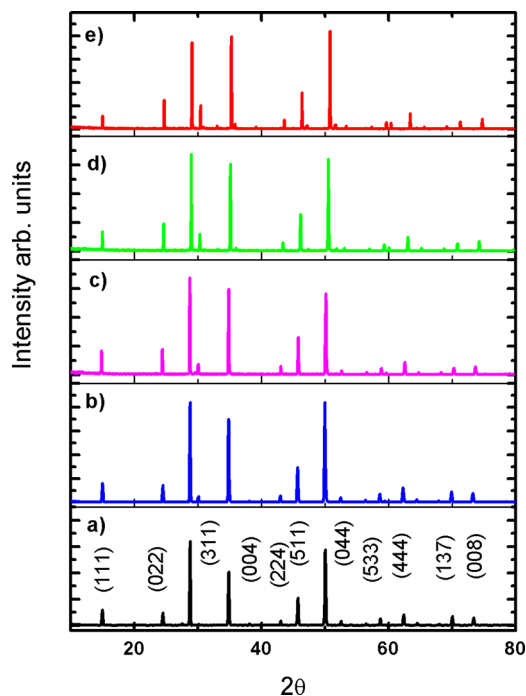


Figure 2. X-ray powder diffraction patterns for (a) $\text{CuCr}_{1.2}\text{Sn}_{0.8}\text{S}_2\text{Se}_2$, (b) $\text{CuCr}_{1.4}\text{Sn}_{0.6}\text{S}_2\text{Se}_2$, (c) $\text{CuCr}_{1.6}\text{Sn}_{0.4}\text{S}_2\text{Se}_2$, (d) $\text{CuCr}_{1.8}\text{Sn}_{0.2}\text{S}_2\text{Se}_2$, and (e) $\text{CuCr}_{1.0}\text{Sn}_{1.0}\text{S}_2\text{Se}_2$ at room temperature.

reasonable values. For example, $\text{CuCr}_{1.4}\text{Sn}_{0.6}\text{S}_2\text{Se}_2$ showed *R*-values of $R_p \sim 5.0\%$ and $R_{\text{exp}} \sim 4.0\%$. The cell lattice parameters increased gradually with increasing Sn concentration (*x*), in accordance with Vegard's law (Figure S3), and compared well with the *a* lattice constant from the single-crystal XRD experiments. These results confirmed that the powder samples crystallized in the normal spinel-type structure. The scanning electron microscopy (SEM) technique was used to analyze the samples (powder and single crystals). The backscattered images and the EDS elemental maps show a uniform distribution of Cu, Cr, Sn and chalcogenide atoms in the samples (Figure S4).

Brüesch and D'Ambrogio⁴² conducted a detailed Raman analysis of nonsubstituted CdCr_2S_4 and CdCr_2Se_4 , in which they assigned the signals to the corresponding symmetry modes characteristic of the spinel crystal structure with space group $Fd\bar{3}m$. According to the irreducible representation of the O_h point group, a set of five Raman-active modes is given by $\Gamma_R = A_{1g} + E_g + 3F_{2g}$. Figure 3 shows the Raman spectra of the

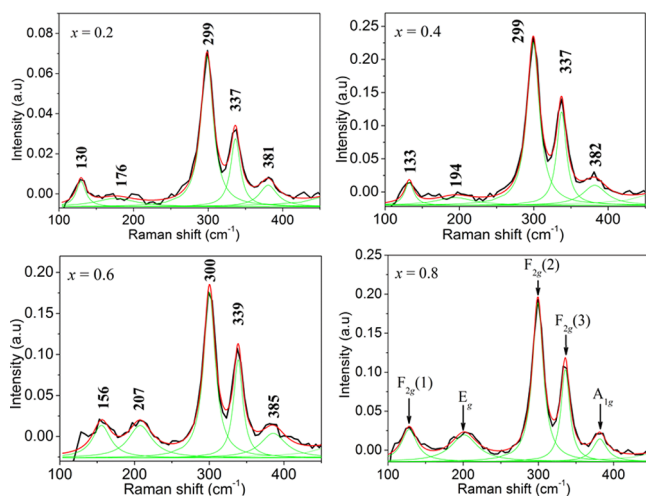


Figure 3. Raman spectra of $\text{CuCr}_{2-x}\text{Sn}_x\text{S}_2\text{Se}_2$ powder samples with the different contributions as deduced from the fitting of the different peaks with Lorentzian curves (green lines). The spectrum for $x = 0.8$ shows the corresponding symmetry modes.

$(\text{Cu})_{\text{tet}}[\text{Cr}_{2-x}\text{Sn}_x]_{\text{oct}}\text{S}_2\text{Se}_2$ ($0.2 \leq x \leq 1.0$) materials collected in the range between 100 and 450 cm^{-1} , where the most important changes were observed.

The spectra, which are characterized by the presence of five signals at approximately 130, 190, 299, 337, and 382 cm^{-1} , compare very well to the spectra of ACr_2X_4 spinels ($A = \text{Cd, Hg, Cu, or Zn}$ and $X = \text{S or Se}$)^{42–48} and $\text{CuCr}_{2-x}\text{Sn}_x\text{S}_4$ spinels, with tin substitution in octahedral positions.⁴⁹ The signals undergo a shift at higher vibrational frequencies with respect to the end-members, as shown in Table 2. Comparative spectra are shown in Figure S5.

The signal at $\sim 382 \text{ cm}^{-1}$ was assigned to the A_{1g} mode, which is attributed to symmetrical stretching of the chalcogen bond with respect to the tetrahedral metal.^{42,43,48,49} The significant shift at higher frequencies was attributed to the random substitution of Se in the 32e sites by S, which changed the polarities of the affected bonds. The band at $\sim 130 \text{ cm}^{-1}$ assigned to the $F_{2g}(1)$ mode was attributed to the translational movement of the CuX_4 tetrahedron, whereas the band at $\sim 299 \text{ cm}^{-1}$ was assigned to the $F_{2g}(2)$ mode corresponding to asymmetric stretching.⁴⁹

Table 2. Frequency and Proposed Mode Assignment of Raman Peaks from Solid Solutions $\text{CuCr}_{2-x}\text{Sn}_x\text{S}_2\text{Se}_2$, $\text{CuCr}_{2-x}\text{Sn}_x\text{S}_4$, and ACr_2X_4 ($A = \text{Cd}, \text{Cu}$ and $X = \text{S}, \text{Se}$) End-Members

mode	CdCr_2S_4 ^{42–45}	CdCr_2Se_4 ⁴²	CuCr_2Se_4 ⁴⁷	$\text{CuCr}_{2-x}\text{Sn}_x\text{S}_4$ ^{49,a}	$\text{CuCr}_{2-x}\text{Sn}_x\text{S}_2\text{Se}_2$ (this work)				
					$x = 0.2$	$x = 0.4$	$x = 0.6$	$x = 0.8$	$x = 1.0$
F_{2g} (1)	101	84	108	130	130	133	156	128	124
E_g	256	154	144	170	176	194	207	201	
F_{2g} (2)	280	169	170	300	299	299	300	299	295
F_{2g} (3)	351	225	220	340	337	337	339	336	338
A_{1g}	394	237	227	400	381	382	385	382	

^aAverage values of the Raman peaks for chemical compositions $x = 0.4, 0.8, 1.0$, and 1.4 .

In contrast, the E_g and F_{2g} (3) modes at ~ 190 and ~ 337 cm^{-1} , respectively, were assigned to the symmetric and antisymmetric twisting of X in the Cr/Sn–X bond at the B sites in $(\text{A})_{\text{tet}}[\text{B}_2]_{\text{oct}}\text{X}_4$.^{42,43,49} The signal at ~ 190 cm^{-1} corresponding to the E_g mode shifted to a wavenumber between those of the spinel end-members (Table 2). This shift was attributed to the random substitution of Cr by Sn atoms at the B position in the 16d sites.⁴⁹ Brüesch and D'Ambrogio have reported that although the force constants of Se and S spinels differ slightly, the force constants of the Cr–X bonds are very similar, regardless of the metal occupying the tetrahedral position.⁴² Based on this assertion, we suggest that the $[\text{B}]_{\text{oct}}\text{–X}$ bonds in our samples should have similar characteristics.

3.3. Magnetic Properties and DFT Calculations. The ZFC/FC magnetization cycles, as a function of temperature for the $(\text{Cu})_{\text{tet}}[\text{Cr}_{2-x}\text{Sn}_x]_{\text{oct}}\text{S}_2\text{Se}_2$ ($x = 0.2, 0.4, 0.6, 0.8$, and 1.0) samples, are shown in Figure 4 and Figure S6. The inset shows

the temperature dependence of the inverse susceptibility ($1/\chi$) fitted by the classical Curie–Weiss law, $\chi = C/(T - \theta)$. The magnetic parameters are listed in Table 3.

Table 3. Magnetic Parameters Spinel Compounds

compounds	T_N, T_C (K)	μ_{eff} (μ_B)	θ (K)	μ_{theo} (μ_B)
$\text{CuCr}_{1.0}\text{Sn}_{1.0}\text{S}_2\text{Se}_2$	18.82	3.99	−36.00	3.87
$\text{CuCr}_{1.2}\text{Sn}_{0.8}\text{S}_2\text{Se}_2$	27.25	4.12	+29.46	4.07
$\text{CuCr}_{1.4}\text{Sn}_{0.6}\text{S}_2\text{Se}_2$	36.75	4.49	+111.47	4.26
$\text{CuCr}_{1.6}\text{Sn}_{0.4}\text{S}_2\text{Se}_2$	191.1	4.69	+189.44	4.45
$\text{CuCr}_{1.8}\text{Sn}_{0.2}\text{S}_2\text{Se}_2$	266.7	4.97	+261.27	4.62

The samples with $x = 0.2$ and 0.4 exhibited ferromagnetic behavior, which was characterized by a high transition temperature (Table 3) determined from the linear extrapolation of $\chi_M(T)$ to zero magnetization.⁵⁰ This behavior has also been observed in $(\text{Cu})_{\text{tet}}[\text{Cr}_{2-x}\text{Sn}_x]_{\text{oct}}\text{Se}_4$ selenospinel phases with low Sn contents.¹⁷ AF behavior was observed in the samples with $x = 0.6, 0.8$, and 1.0 , with Néel temperatures (T_N) of 18.8, 27.3, and 36.7 K, respectively. The samples with $x = 0.6$ and 0.8 had positive θ values (Table 3), which suggested that the exchange interactions had a dominant ferromagnetic character superimposed on AF interactions. When Cr atoms are substituted by Sn atoms in end-member phases, the ferromagnetic components are partially inhibited, whereas the antiferromagnetic components are promoted.

For $\text{CuCrSnS}_2\text{Se}_2$, the lattice parameters obtained by means of DFT calculations are in good agreement with the experimental values of the single-crystal X-ray diffraction, with a maximum difference of 1.3% observed for the c -axis ($a = 10.509$ Å, $b = 10.474$ Å, $c = 10.544$ Å, $\alpha = 90.1^\circ$, $\beta = 89.0^\circ$, and $\gamma = 89.9^\circ$). These small Jahn–Teller distortions break the degeneration of the energy levels and therefore diminish the energy of the system. Figure 1b shows the crystalline structure obtained, with polyhedrons containing central Cr (red tetrahedron), Sn (gray tetrahedron), and Cu (blue octahedron) atoms. The $[\text{Cr}/\text{Sn}]$ –Se bond distances ranged from 2.50 to 2.66 Å. The ELD indices of $[\text{Cr}]\text{X}_6$ and $[\text{Sn}]\text{X}_6$ were in the range of 2.4–3.1%. These calculated bond distances and distortion indices compare very well those obtained from the single-crystal X-ray diffraction data. Inspection of the electronic localization function (ELF) of $\text{CuCr}_{1.0}\text{Sn}_{1.0}\text{S}_2\text{Se}_2$ revealed a minimum in the electronic density at the position where Sn is in the tetravalent state with a high-spin configuration (Figure 5).

The effective magnetic moments for $(\text{Cu})_{\text{tet}}[\text{Cr}_{2-x}\text{Sn}_x]_{\text{oct}}\text{S}_2\text{Se}_2$ obtained from the experimental magnetic measurements were similar to those expected for $\text{Cu}^{1+}[\text{Cr}_{1.0}^{3+}\text{Cr}_{(1-x)}^{4+}\text{Sn}_x^{4+}]\text{S}_2\text{Se}_2$ (Table 3). The theoretical calculated magnetic moments (μ_{theo}) clearly demonstrated that

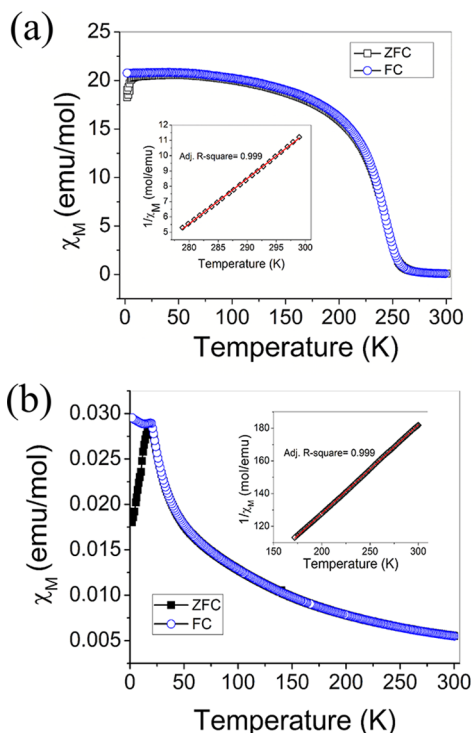


Figure 4. ZFC/FC magnetization cycles measured for $\text{CuCr}_{1.8}\text{Sn}_{0.2}\text{S}_2\text{Se}_2$ (a) and $\text{CuCr}_{1.0}\text{Sn}_{1.0}\text{S}_2\text{Se}_2$ (b) powder samples at $H_{\text{app}} = 500$ Oe. The inset shows the $1/\chi$ as a function of temperature in the paramagnetic regime fitted with the classical Curie–Weiss expression, where the temperature range varied depending on the compound.

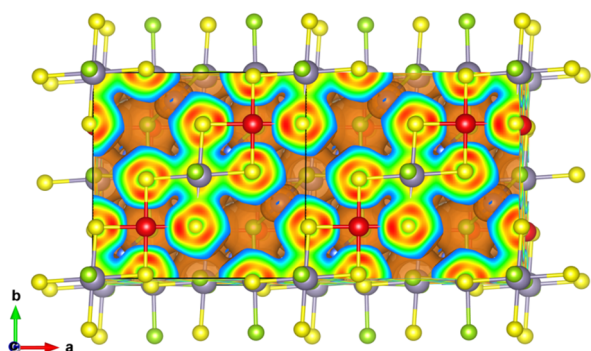


Figure 5. Electronic localization function (ELF) for $\text{CuCr}_{1.0}\text{Sn}_{1.0}\text{S}_2\text{Se}_2$ obtained by DFT calculations. The red, gray, green, and yellow spheres represent Cr, Sn, Se, and S atoms, respectively. The orange areas illustrate the positions in the cage with the minimum electronic density.

Sn shows diamagnetic behavior with an oxidation state of 4+. These results are well correlated to the models of $(\text{Cu})_{\text{tet}}[\text{Cr}_{2-x}\text{M}_x]_{\text{oct}}\text{Se}_4$ spinels, where M and Cu exist in the 4+ and 1+ oxidation states, respectively.^{12,13,18–20}

DFT calculations for $\text{CuCr}_{1.0}\text{Sn}_{1.0}\text{S}_2\text{Se}_2$ revealed that the most stable magnetic state is AF with a magnetic moment of $2.90 \mu_{\text{B}}$ for each Cr atom (within a Wigner–Seitz radius of 1.3 Å) and an energy of 269 meV lower than that of the ferromagnetic state. A schematic representation of the magnetic state of $\text{CuCr}_{1.0}\text{Sn}_{1.0}\text{S}_2\text{Se}_2$ is shown in Figure 6.

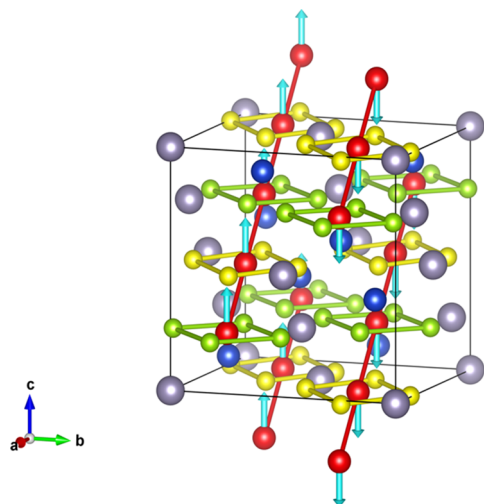


Figure 6. Magnetic configuration for $\text{CuCr}_{1.0}\text{Sn}_{1.0}\text{S}_2\text{Se}_2$ obtained by DFT calculations. The red, gray, blue, green, and yellow spheres represent Cr, Sn, Cu, Se, and S atoms, respectively.

It can be seen that a magnetic structure of Cr atoms is formed by ferromagnetic chains in the $[101]$ direction with a first-neighbor distance of 3.69 Å. The second-neighbor distance between the Cr atoms is 6.44 Å, which is an AF interaction, and the third-neighbor distance is 7.43 Å, which is also an AF interaction. The exchange constant obtained for the interaction with first neighbors is $J_1 = 56.22 \text{ cm}^{-1}$ (80.8 K), whereas that with second neighbors is $J_2 = -33.88 \text{ cm}^{-1}$ (−48.7 K). The exchange constants for superexchange and double-exchange interactions were calculated for $\text{CuCr}_{1-x}\text{Hf}_x\text{Se}_4$ using the tight-binding approach.⁵¹ Ferromagnetic $\text{CuCr}_{1.81}\text{Hf}_{0.14}\text{Se}_4$ showed values of $J_{aa} = 61.5 \text{ K}$ and $J_{ab} =$

−8.23 K, where J_{aa} and J_{ab} correspond to the superexchange integrals. Maciążek et al. proposed stabilization of the double-exchange and superexchange interactions between the Cr^{3+} and Cr^{4+} cations and the presence of Hf^{4+} cations in the octahedral sites: $\text{Cu}^{1+}[\text{Cr}_{1.0}^{3+}\text{Cr}_{(1-x)}^{4+}\text{Hf}_x^{4+}]\text{Se}_4^{2-}$.⁵¹ Thus, the AF interaction between the different ferromagnetic chains for $\text{CuCr}_{1.0}\text{Sn}_{1.0}\text{S}_2\text{Se}_2$ (our work) originates from the presence of diamagnetic Sn cations, producing a transfer of the majority and minority spins contrary to those of the chalcogen bonds.

4. CONCLUSIONS

Single crystals of $\text{CuCr}_{1.0}\text{Sn}_{1.0}\text{S}_{2.1}\text{Se}_{1.9}$, $\text{CuCr}_{1.2}\text{Sn}_{0.8}\text{S}_{2.1}\text{Se}_{1.9}$, $\text{CuCr}_{1.3}\text{Sn}_{0.7}\text{S}_{2.2}\text{Se}_{1.8}$ and $\text{CuCr}_{1.5}\text{Sn}_{0.5}\text{S}_{2.2}\text{Se}_{1.8}$ were synthesized by the conventional solid-state method. They crystallize in normal spinel-type structures as determined by single-crystal X-ray diffraction. The backscattered images and the EDS elemental analyses showed a uniform distribution of Cu, Cr, Sn, and chalcogenide atoms in the samples (powder and single crystals). The vibrational analysis showed that the A_{1g} , E_g and three F_{2g} modes were Raman-active, in good agreement with the spectra of the spinel ACr_2X_4 end-members. The PXRD patterns and Rietveld refinement results for the polycrystalline ($0.2 \leq x \leq 1.0$) materials are in close agreement with those obtained from single-crystal X-ray diffraction. The magnetic susceptibility measurements of $(\text{Cu})_{\text{tet}}[\text{Cr}_{2-x}\text{Sn}_x]_{\text{oct}}\text{S}_2\text{Se}_2$ showed an evolution from ferromagnetic behavior for $x = 0.2$ to predominantly AF behavior when $x = 1.0$. The theoretical DFT calculations, μ_{eff} and μ_{theo} values clearly demonstrate that Sn was a diamagnetic cation with an oxidation state of 4+ and an effective moment close to that expected for $(\text{Cu}^{1+})_{\text{tet}}[\text{Cr}_{2-x}^{3+}\text{Sn}_x^{4+}]_{\text{oct}}\text{S}_2\text{Se}_2$. DFT calculations suggested that decreasing the ferromagnetic chains, associated with the chemical substitution of Cr by Sn in $(\text{Cu})_{\text{tet}}[\text{Cr}_2]_{\text{oct}}\text{S}_2\text{Se}_2$ stimulates AF interactions. Thus, the ferromagnetic chains are connected by AF interactions.

■ ASSOCIATED CONTENT

Supporting Information

The Supporting Information is available free of charge on the ACS Publications website at DOI: 10.1021/acs.inorgchem.9b01853.

Atomic coordinates, SEM and mapping of single crystal and powder pattern, Rietveld refinement, Vegard Law, comparative Raman in powder samples, and zero-field-cooled (ZFC)/field-cooled (FC) magnetization cycles (PDF)

Accession Codes

CCDC 1935201, 1935203, and 1935209–1935210 contain the supplementary crystallographic data for this paper. These data can be obtained free of charge via www.ccdc.cam.ac.uk/data_request/cif, or by emailing data_request@ccdc.cam.ac.uk, or by contacting The Cambridge Crystallographic Data Centre, 12 Union Road, Cambridge CB2 1EZ, UK; fax: +44 1223 336033.

■ AUTHOR INFORMATION

Corresponding Authors

*E-mail pbaraho@ucm.cl.

*E-mail agaldamez@uchile.cl.

ORCID

Antonio Galdámez: 0000-0001-9665-7696

Author Contributions

The manuscript was written through contributions of all authors. All authors have given approval to the final version of the manuscript and contributed equally.

Notes

The authors declare no competing financial interest.

ACKNOWLEDGMENTS

This work was supported by FONDECYT Grant 1161020, the Chilean-French International Associated Laboratory for “Multifunctional Molecules and Materials” (LIAM3-CNRS No. 1027), and “Financiamiento Basal para Centros Científicos y Tecnológicos de Excelencia FB 0807”. The authors are grateful to Thierry Guizouarn (Université de Rennes 1, France) for magnetic characterization and Thierry Roisnel (Centre de Diffractométrie X CDIFX), Université de Rennes 1, France) for collection of the X-ray data for the $\text{CuCr}_{1.0}\text{Sn}_{1.0}\text{S}_{2.1}\text{Se}_{1.9}$ and $\text{CuCr}_{1.2}\text{Sn}_{0.8}\text{S}_{2.1}\text{Se}_{1.9}$ single-crystals. The authors also thank the FONDEQUIP Grant EQM140142 for Raman Witec Alpha 300 equipment.

REFERENCES

- (1) Sickafus, K. E.; Wills, J. M.; Grimes, N. W. Structure of Spinel. *J. Am. Ceram. Soc.* **1999**, *82*, 3279–3292.
- (2) Biagioni, C.; Pasero, M. The Systematics of the Spinel-Type Minerals: An Overview. *Am. Mineral.* **2014**, *99*, 1254–1264.
- (3) Ito, M.; Furuta, T.; Terada, N.; Ebisu, S.; Nagata, S. Relaxation of Magnetization in Spinel CuCrZrS_4 . *Phys. B* **2012**, *407*, 1272–1274.
- (4) Ito, M.; Kado, N.; Matsubayashi, K.; Uwatoko, Y.; Terada, N.; Ebisu, S.; Nagata, S. Magnetic Properties of Spinel CuCrZrS_4 under Pressure. *J. Magn. Magn. Mater.* **2013**, *331*, 98–101.
- (5) Manjon, F. J.; Tiginyanu, I.; Ursaki, V. *Pressure-Induced Phase Transitions in AB_2X_4 Chalcogenide Compounds*; Springer-Verlag: Berlin, Germany, 2014; Vol. 189.
- (6) Ramirez, A. P.; Cava, R. J.; Krajewski, J. Colossal Magnetoresistance in Cr-Based Chalcogenide Spinel. *Nature* **1997**, *386*, 156–159.
- (7) Krohns, S.; Schrette, F.; Lunkenheimer, P.; Tsurkan, V.; Loidl, A. Colossal Magnetocapacitive Effect in Differently Synthesized and Doped CdCr_2S_4 . *Phys. B* **2008**, *403*, 4224–4227.
- (8) Fujimoto, Y.; Fujita, T.; Mitsudo, S.; Idehara, T.; Kawashima, Y.; Nagata, S. High-Frequency ESR Studies of Colossal Magnetoresistance System $\text{Cu}(\text{Cr}_{1-x}\text{Zr}_x)_2\text{S}_4$. *J. Magn. Magn. Mater.* **2007**, *310*, 1991–1993.
- (9) Alvaro, M.; Nestola, F.; Ross, N.; Domeneghetti, C.; Reznitsky, L. High-Pressure Behavior of Thiospinel CuCr_2S_4 . *Am. Mineral.* **2014**, *99*, 908–913.
- (10) Efthimiopoulos, I.; Tsurkan, V.; Loidl, A.; Zhang, D.; Wang, Y. Comparing the Pressure-Induced Structural Behavior of CuCr_2O_4 and CuCr_2Se_4 Spinels. *J. Phys. Chem. C* **2017**, *121*, 16513–16520.
- (11) Saha-Dasgupta, T.; De Raychaudhury, M.; Sarma, D. D. Ferromagnetism in Metallic Chalcospinel CuCr_2S_4 and CuCr_2Se_4 . *Phys. Rev. B* **2007**, *76*, 054441.
- (12) Kimura, A.; Matsuno, J.; Okabayashi, J.; Fujimori, A.; Shishidou, T.; Kulatov, E.; Kanomata, T. Soft X-Ray Magnetic Circular Dichroism Study of the Ferromagnetic Spinel-Type Cr Chalcogenides. *Phys. Rev. B: Condens. Matter Mater. Phys.* **2001**, *63*, 224420.
- (13) Lotgering, F. K. Ferromagnetism in Spinels: CuCr_2S_4 and CuCr_2Se_4 . *Solid State Commun.* **1964**, *2*, 55–56.
- (14) Furubayashi, T.; Suzuki, H.; Kobayashi, N.; Nagata, S. Large Negative Magnetoresistance in Thiospinel CuCrZrS_4 . *Solid State Commun.* **2004**, *131*, 505–508.
- (15) Kariya, F.; Ebisu, S.; Nagata, S. Evolution from a Ferromagnetic to a Spin-Glass Regime in the Spinel-Type $\text{Cu}(\text{Cr}_{1-x}\text{Ti}_x)_2\text{S}_4$. *J. Solid State Chem.* **2009**, *182*, 608–616.
- (16) Barahona, P.; Galdámez, A.; López-Vergara, F.; Manríquez, V.; Peña, O. Crystal Structure and Magnetic Properties of Titanium-Based $\text{CuTi}_{2-x}\text{M}_x\text{S}_4$ and $\text{CuCr}_{2-x}\text{Ti}_x\text{Se}_4$ Chalcospinel. *J. Solid State Chem.* **2014**, *212*, 114–120.
- (17) Pinto, C.; Galdámez, A.; Barahona, P.; Moris, S.; Peña, O. Crystal Structure, Raman Scattering and Magnetic Properties of $\text{CuCr}_{2-x}\text{Zr}_x\text{Se}_4$ and $\text{CuCr}_{2-x}\text{Sn}_x\text{Se}_4$ Selenospinel. *J. Magn. Magn. Mater.* **2018**, *456*, 160–166.
- (18) Belakroum, K.; Ouili, Z.; Leblanc-Soreau, A.; Hemmida, M.; Krug von Nidda, H.-A. Magnetic Properties of CuCrZrSe_4 . *J. Magn. Magn. Mater.* **2013**, *334*, 130–135.
- (19) Yamamoto, H.; Kawashima, Y.; Hondou, K.; Ebisu, S.; Nagata, S. Spin-Liquid Behavior in the Spinel-Type $\text{Cu}(\text{Cr}_{1-x}\text{Zr}_x)_2\text{S}_4$. *J. Magn. Magn. Mater.* **2007**, *310*, e426–e428.
- (20) Iijima, Y.; Kamei, Y.; Kobayashi, N.; Awaka, J.; Iwasa, T.; Ebisu, S.; Chikazawa, S.; Nagata, S. A New Ferromagnetic Thiospinel CuCrZrS_4 with Re-Entrant Spin-Glass Behaviour. *Philos. Mag.* **2003**, *83*, 2521–2530.
- (21) Pankrats, A. I.; Vorotynov, A. M.; Tugarinov, V. I.; Zharkov, S. M.; Zeer, G. M.; Ramasamy, K.; Gupta, A. Magnetic Resonance Studies of Mixed Chalcospinel $\text{CuCr}_2\text{S}_4\text{Se}_{4-x}$ ($x = 0; 2$) and $\text{Co}_x\text{Cu}_{1-x}\text{Cr}_2\text{S}_4$ ($x = 0.1; 0.2$) Nanocrystals with Strong Interparticle Interactions. *J. Magn. Magn. Mater.* **2018**, *452*, 297–305.
- (22) Koroleva, L. I. Antiferromagnetic States of Charge Carriers in the Ferromagnetic Semiconductors $\text{CuCr}_2\text{S}_{4-x}\text{Se}_x$ ($0.5x < 1.5$) with Curie Points above Room Temperature. *J. Exp. Theor. Phys.* **1994**, *79*, 153–162.
- (23) Tsuji, S.; Kumagai, K.; Matsumoto, N.; Nagata, S. Metal-Insulator Transition in the Spinel $\text{CuIr}_2(\text{S}_{1-x}\text{Se}_x)_4$ System Studied by NMR. *Phys. C* **1997**, *282–287*, 1107–1108.
- (24) Gogoowicz, M.; Juszczak, S.; Warczewski, J.; Mydlarz, T. Ferrimagnetism of $\text{Cu}_{0.45}\text{Co}_{0.55}\text{Cr}_2\text{S}_{4-y}\text{Se}_y$. *Phys. Rev. B: Condens. Matter Mater. Phys.* **1987**, *35*, 7073–7080.
- (25) Bruker Analytical X-Ray Instruments Inc. SMART, SAINT-PLUS V6.02, SHELXTL V6.10, and SADABS; Bruker Analytical X-Ray Instruments Inc.: Madison, WI, 2015.
- (26) Sheldrick, G. M. SHELXL-97, Program for the Refinement of Crystal Structures; University of Göttingen: Stuttgart, Germany, 1997.
- (27) Dolomanov, O. V.; Bourhis, L. J.; Gildea, R. J.; Howard, J. A. K.; Puschmann, H. OLEX2: A Complete Structure Solution, Refinement and Analysis Program. *J. Appl. Crystallogr.* **2009**, *42*, 339–341.
- (28) Lutterotti, L. Total Pattern Fitting for the Combined Size - Strain - Stress - Texture Determination in Thin Film Diffraction. *Nucl. Instrum. Methods Phys. Res., Sect. B* **2010**, *268*, 334–340.
- (29) Kresse, G.; Hafner, J. Ab Initio Molecular Dynamics for Liquid Metals. *Phys. Rev. B: Condens. Matter Mater. Phys.* **1993**, *47*, 558–561.
- (30) Kresse, G.; Furthmüller, J. Efficiency of Ab-Initio Total Energy Calculations for Metals and Semiconductors Using a Plane-Wave Basis Set. *Comput. Mater. Sci.* **1996**, *6*, 15–50.
- (31) Hohenberg, P.; Kohn, W. Inhomogeneous Electron Gas. *Phys. Rev.* **1964**, *136*, B864–B871.
- (32) Kohn, W.; Sham, L. Self-Consistent Equations Including Exchange and Correlation Effects. *Phys. Rev.* **1965**, *140*, A1133–A1138.
- (33) Kresse, G.; Joubert, D. From Ultrasoft Pseudopotentials to the Projector Augmented-Wave Method. *Phys. Rev. B: Condens. Matter Mater. Phys.* **1999**, *59*, 1758–1775.
- (34) Kresse, G.; Hafner, J. Norm-Conserving and Ultrasoft Pseudopotentials for First-Row and Transition Elements. *J. Phys.: Condens. Matter* **1994**, *6*, 8245–8257.
- (35) Perdew, J. P.; Burke, K.; Ernzerhof, M. Generalized Gradient Approximation Made Simple. *Phys. Rev. Lett.* **1996**, *77*, 3865–3868.
- (36) Monkhorst, H. J.; Pack, J. D. Special Points for Brillouin-Zone Integrations. *Phys. Rev. B* **1976**, *13*, 5188–5192.
- (37) Riedel, E.; Morlock, W. Röntgenographische Und Elektronische Eigenschaften, MoBbauer- Und I R-Spektren Des Spinellsystems $\text{CuCrSn}(\text{S}_{1-x}\text{Se}_x)_4$. *Z. Anorg. Allg. Chem.* **1978**, *438*, 233–241.

- (38) Mähl, D.; Pickardt, J.; Reuter, B. Züchtung Und Untersuchung von Einkristallen Der Verbindungen CuCrZrSe_4 Und CuCrSnSe_4 . *Z. Anorg. Allg. Chem.* **1984**, 508, 197–200.
- (39) Shannon, R. D. Revised Effective Ionic Radii and Systematic Studies of Interatomic Distances in Halides and Chalcogenides. *Acta Crystallogr., Sect. A: Cryst. Phys., Diffr., Theor. Gen. Crystallogr.* **1976**, 32, 751–767.
- (40) Pyykko, P. Refitted Tetrahedral Covalent Radii for Solids. *Phys. Rev. B: Condens. Matter Mater. Phys.* **2012**, 85, 024115.
- (41) Baur, W. H. The Geometry of Polyhedral Distortions. Predictive Relationships for the Phosphate Group. *Acta Crystallogr., Sect. B: Struct. Crystallogr. Cryst. Chem.* **1974**, 30, 1195–1215.
- (42) Brüesch, P.; D'Ambrogio, F. Lattice Dynamics and Magnetic Ordering in the Chalcogenide Spinel CdCr_2S_4 and CdCr_2Se_4 . *Phys. Status Solidi B* **1972**, 50, 513–526.
- (43) Gnezdilov, V.; Lemmens, P.; Pashkevich, Y. G.; Payen, C.; Choi, K. Y.; Hemberger, J.; Loidl, A.; Tsurkan, V. Phonon Anomalies and Possible Local Lattice Distortions in Giant Magnetocapacitive CdCr_2S_4 . *Phys. Rev. B: Condens. Matter Mater. Phys.* **2011**, 84, 045106.
- (44) Koshizuka, N.; Ushioda, S.; Tsushima, T. Resonance Raman Scattering in CdCr_2S_4 . Magnetic-Circular-Polarization Properties. *Phys. Rev. B: Condens. Matter Mater. Phys.* **1980**, 21, 1316–1322.
- (45) Fennie, C. J.; Rabe, K. M. Polar Phonons and Intrinsic Dielectric Response of the Ferromagnetic Insulating Spinel CdCr_2S_4 from First Principles. *Phys. Rev. B: Condens. Matter Mater. Phys.* **2005**, 72, 214123.
- (46) Efthimiopoulos, I.; Yaresko, A.; Tsurkan, V.; Deisenhofer, J.; Loidl, A.; Park, C.; Wang, Y. Multiple Pressure-Induced Transitions in HgCr_2S_4 . *Appl. Phys. Lett.* **2013**, 103, 201908.
- (47) Ivanov, V. G.; Iliev, M. N.; Wang, Y. H. A.; Gupta, A. Ferromagnetic Spinel CuCr_2Se_4 Studied by Raman Spectroscopy and Lattice Dynamics Calculations. *Phys. Rev. B: Condens. Matter Mater. Phys.* **2010**, 81, 224302.
- (48) Bruesch, P.; Schuler, C. Raman and infrared spectra of crystal with $\alpha\text{-NaFeO}_2$ structure. *J. Phys. Chem. Solids* **1971**, 32, 1025–1038.
- (49) Valencia-Gálvez, P.; Peña, O.; Moris, S.; Barahona, P. Raman characterization of $\text{CuCr}_{2-x}\text{Sn}_x\text{S}_4$ spinels. *J. Chil. Chem. Soc.* **2019**, 64, 4285–4289.
- (50) Oumezzine, M.; Zemni, S.; Peña, O. Room Temperature Magnetic and Magnetocaloric Properties of $\text{La}_{0.67}\text{Ba}_{0.33}\text{Mn}_{0.98}\text{Ti}_{0.02}\text{O}_3$ Perovskite. *J. Alloys Compd.* **2010**, 508, 292–296.
- (51) Maciążek, E.; Malicka, E.; Gagor, A.; Stokłosa, Z.; Groń, T.; Sawicki, B.; Duda, H.; Gudwański, A. Semiconducting-Metallic Transition of Singlecrystalline Ferromagnetic Hf-Doped CuCr_2Se_4 Spinel. *Phys. B* **2017**, 520, 116–122.